



Design and energy absorption performance of a new jigsaw-inspired multi-directional self-locking system



Yao-Yao Xu ^{a,b}, Jin-Shui Yang ^{a,b,*} , Hao Han ^{a,b}, Peng Yin ^{a,b}, Shuang Li ^{a,b}, Xu-Chang Liu ^{a,b}, Hong-Ze Li ^{a,b}, Jing Gao ^{a,b}

^a Harbin Engineering University, Harbin 150001 PR China

^b Qingdao Innovation and Development Center of Harbin Engineering University, Qingdao 266000 PR China

ARTICLE INFO

Keywords:
Self-locking system
Multi-directional
Energy absorption
Deformation modes

ABSTRACT

The self-locking system interlocks with the adjacent cell without additional constraints upon loading, featuring convenient assembly and easy replacement after damage. However, conventional self-locking systems typically offer limited single-directional self-locking performance. In this study, inspired by the jigsaw puzzle, a jigsaw-inspired multi-directional self-locking system (JMSS) comprising concave and convex cells is designed. Thanks to the excellent symmetry of the system, the cells become fully interlocked when loaded in all directions on the surface, and the JMSS exhibits multi-directional load-bearing and energy absorbing capabilities. The deformation modes and energy absorption characteristics of two types of single cells and the JMSS are obtained through quasi-static compression tests, and their results are compared, demonstrating that the JMSS exhibits superior mechanical properties and energy absorption characteristics. Methods of foam-filling and tube-filling are used to explore the enhancement effects of both methods for single cells and the JMSS. Finally, the impact of geometric parameters on the mechanical properties of the system is assessed and compared with the traditional systems, demonstrating that JMSS possesses better multi-directional self-locking properties.

1. Introduction

Lightweight structures are extensively utilized in various engineering fields such as aerospace, marine, and automotive due to their excellent properties, including high specific strength, high specific stiffness, and energy absorption capacity [1–4]. Researchers have proposed diverse lightweight structures such as honeycomb, lattice, grid, and origami structures. By optimizing the design of the basic cell elements, these structures can be made to exhibit exceptional metamaterial mechanical and energy absorption properties such as negative Poisson's ratio [5–7], negative stiffness [8–10] and ultra-stiff [11–13].

The advent of advanced fabrication technologies, particularly 3D printing, has expanded the possibilities for designing and manufacturing complex lightweight structures. These technologies enable precise control over cell geometries, which is crucial for tailoring mechanical properties [14–17]. Acanfora et al. [18] demonstrated that 3D printing combined with composite carbon fiber panels can reduce structural density by 28 %. Wang et al. [19] showed that integrating concave hexagonal and star-shaped negative Poisson's ratio structures can

significantly enhance energy absorption. Other researchers have focused on improving specific mechanical behaviors through the development of chiral metamaterials, curved beam reinforcement, and pyramidal arrays [20–24]. In addition to material and fabrication innovations, foam-filled and tube-filled structures have emerged as prominent methods for enhancing the energy absorption of lightweight designs. Foam materials, known for their low density and high energy absorption, are frequently used to fill thin-walled tubes, significantly improving the structural strength and stiffness [25–30]. Xiang et al. [31] performed a series of compression experiments on tubular structures, identifying key indicators for evaluating their load-bearing and energy absorption properties. Likewise, Yao et al. [32] demonstrated that foam-filling can strengthen negative stiffness structures, while Chen et al. [33] applied bionic principles to tube designs inspired by bamboo, leading to improved crashworthiness.

Lattice structures are commonly used in static load-bearing applications [34–36], such as architectural frameworks and aerospace components, where their efficient load distribution is advantageous. However, they often lack the flexibility needed in dynamic or rapidly

* Corresponding author at: Harbin Engineering University, Harbin 150001, PR China.
E-mail address: yangjinshui@hrbeu.edu.cn (J.-S. Yang).

changing environments. Self-locking systems [37–39], by combining geometric interlocking with scalable assembly processes, provide a versatile solution that can be applied in both dynamic and static environments, offering advantages in fields ranging from temporary structures to energy-absorbing systems in crash scenarios.

Chen et al. [40] first introduced the concept of self-locking systems with a thin-walled metal structure featuring a dumbbell-shaped cross-section. This design allowed the system to self-lock through tube interactions, demonstrating excellent energy absorption capabilities. Subsequent research has focused on theoretical aspects [41], material innovations [42,43], and shape optimization [44,45] to further enhance the performance of dumbbell-shaped tube systems. Chen et al. [46] later developed a bellows-type self-locking system, which improved material utilization and load stability. Zhu et al. [47], inspired by ancient Chinese mortise-and-tenon technology, designed a self-locking system that demonstrates a negative Poisson's ratio effect, combining the advantages of self-locking mechanisms with the exceptional mechanical properties of such materials. Liu et al. [48] proposed a novel design strategy for tubular self-locking systems, which led to the development of various configurations [49,50]. Zhao et al. [51–53] designed a bi-directional self-locking system inspired by origami creases, which significantly improved the system's resistance to oblique impacts. Their research analyzed how different shapes and the number of origami grooves influenced the crushing force and energy absorption.

Current research indicates that self-locking systems possess considerable potential for energy dissipation. However, traditional systems primarily exhibit self-locking properties in a single direction. Inspired by the discrete nature of jigsaws, this study introduces the jigsaw-inspired multi-directional self-locking system (JMSS), integrating both concave

(A-cell) and convex (T-cell) cells. The design enables enhanced load-bearing and energy-absorbing capabilities across multiple directions. To assess the mechanical properties of the JMSS, quasi-static experiments are conducted on two types of hollow cells. These cells are then filled with foam and tubes to evaluate the impact of filling methods on load-bearing capacity and specific energy absorption. Additionally, the effects of wall thickness, web inclination, and depth of concavity/protrusion on the JMSS energy absorption are explored through finite element analysis. Compared with conventional systems, the JMSS demonstrates superior multi-directional performance.

2. JMSS system design

Traditional self-locking systems, such as the dumbbell-shaped tube system (DSTS) [40], corrugated tube system (CGTS) [46], and bidirectional self-locking thin-walled system (BSTS) [51], exhibit self-locking capabilities only in one direction, dispersing under loads from other directions, as shown in Fig. 1(b)–(d). In contrast, the JMSS, composed of concave A-cells and convex T-cells, is designed to interlock across multiple directions, offering comprehensive self-locking performance, as shown in Fig. 1(e). The JMSS, which comprises A-cell and T-cell. The dimensions of a single cell, including length, height, depth of concavity/protrusion, wall thickness, and web inclination angle, are denoted by L , D , h , t , and α , respectively. Additionally, to reduce stress concentration, a rounded transition is implemented at the interlocking positions. Consequently, the transition satisfies the equations $R_1 = R_2 \cdot t$ and $R_2 = R_3 \cdot t$, as illustrated in Fig. 2(b) and (c). The specific geometric parameters of T-cell and A-cell are provided in Table 1.

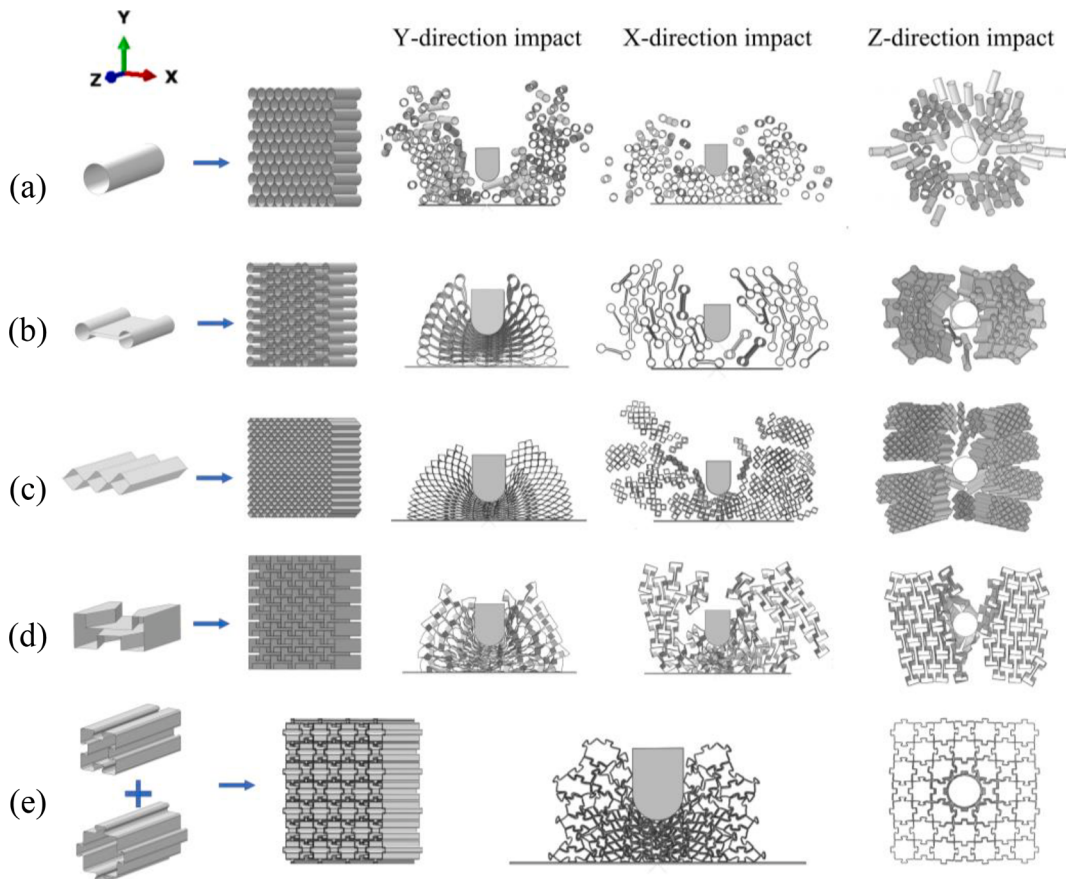


Fig. 1. The behavior of tube, DSTS [40], CGTS [46], BSTS[51], and JMSS under impact loading is as follows: (a) sputtering occurs when the structure is loaded in any direction, (b)–(d) self-locking is achieved by loading in a single direction, with sputtering occurring in other directions, and (e) the JMSS achieves self-locking in all directions.

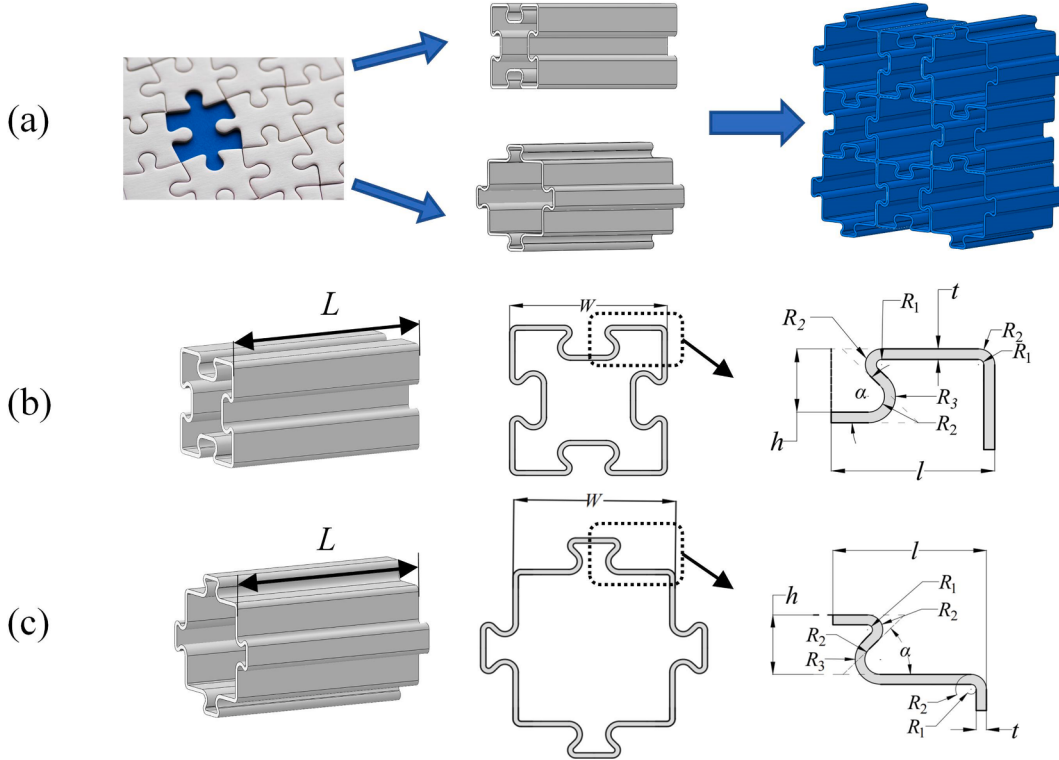


Fig. 2. JMSS-inspired sources and geometric parameters of cells: (a) source of inspiration, (b) A-cell, (c) T-cell.

Table 1

The geometric parameter of A-cell and T-cell (mm).

L	W	h	t	α	l	R_1	R_2	R_3
60	30	6	1.2	45°	15	0.5	1.7	2.3

3. Materials and methods

3.1. Materials and fabrication

Polylactic acid (PLA) is selected as the printing material due to its environmental friendliness and biodegradability. The material of 3D printing is provided by Shenzhen Bambu Technology Companies. The 3D printing process is conducted using fused deposition modeling (FDM), with a nozzle temperature of 210 °C and a build plate temperature maintained between 60 °C and 65 °C. The fill density is set to 60%, and the print path is set according to the contour of the specimen and the 3D structure is printed in the axial direction to ensure structural consistency. The printed specimens are shown in Fig. 3(a). Due to the large number of cavities within the cells, foam and tubes are used to fill the interior, enhancing the load-bearing and energy-absorbing capabilities of the cells. The foam used is polyurethane, primarily composed of toluene diisocyanate and polyether polyol, which are mixed in a 1:1 ratio and poured into the hollow cells to form foam. After curing, excess

foam is removed, as shown in Fig. 3(b). The tube is fabricated from the same PLA material as the cell elements using 3D printing technology. It is cut to fit internally within the T-cell and A-cell, with a wall thickness of 1.2 mm, as shown in Fig. 3(c).

To validate the material properties of PLA, dog bone specimens are fabricated according to GB/T 1040.2–2006 standards. Tensile tests are performed using a universal testing machine (FL5105GD, FULETEST) at a loading rate of 1 mm/min, with an extensometer used to capture the displacement changes in the dog bone specimens. The test results are shown in Fig. 4(a), with the yield stress of PLA calculated using the 0.2 % strain offset rule [31]. The dimensions of the dog bone specimens and the morphology of the fracture after tensile testing are shown in Fig. 4 (b) and (c). The average values of the measured material parameters are used as the final material properties of PLA, as shown in Table 2.

3.2. Experiment

Quasi-static experiments are conducted on the specimens using a compression fixture in the FL5105GD universal testing system. The specimens are placed between the stationary plate and the loading plate, with the latter applying downward loading at a rate of 1 mm/min to minimize dynamic effects. Displacement and force data are recorded via sensors and a data acquisition system, as shown in Fig. 5(a). Initially, quasi-static experiments are performed on hollow T-cell and A-cell specimens. Following this, quasi-static tests are carried out on the JMSS



Fig. 3. Specimens fabricate by 3D printing and filler setups:(a) hollow, (b) foam, (c) tube.

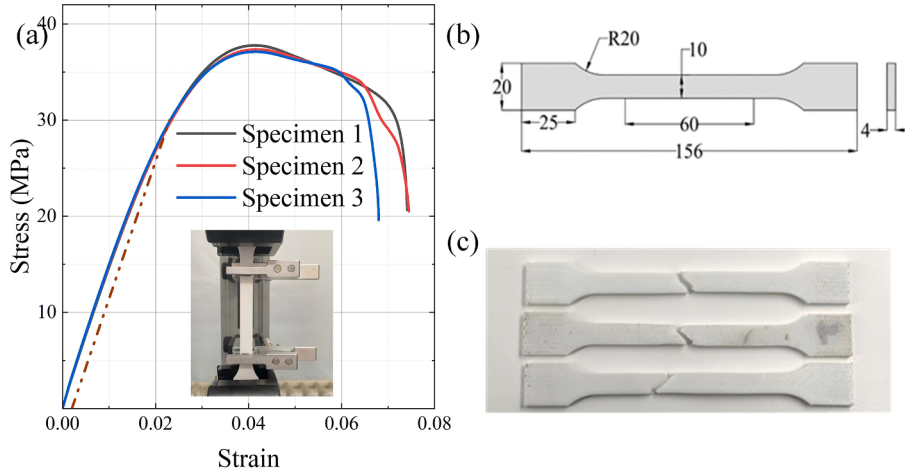


Fig. 4. Mechanical properties of PLA: (a) stress–strain curves of PLA material, (b) geometric parameters of dog-bone, (c) morphology of fracture after stretching.

Table 2
Mechanical properties of PLA.

Young's modulus E (MPa)	Yield stress σ_0 (MPa)	Poisson's ratio ν	Density g/cm ³
1325	30.1	0.25	1.18

under the same loading conditions as those used for the individual cells. Similarly, foam and tubes are used to fill the internal cavities.

To quantitatively analyze the mechanical properties and energy absorption capacity of the JMSS, various key metrics are employed, including total energy absorption (EA), specific energy absorption (SEA), mean crushing force (MCF), and energy absorption efficiency (E_f).

Total energy absorption is mathematically defined as follows:

$$EA = \int_0^{u_d} f(u) d(u) \quad (1)$$

Here, $f(u)$ represents the force in the quasi-static loading process, and u denotes the displacement during compression, u_d represents the displacement at densification, varying according to structural deformation laws as delineated in Eq. (4).

To neutralize mass effects on structural energy absorption, the SEA is evaluated using Eq. (2). This metric divides the total absorbed energy of each specimen by its mass, presenting the absorbed energy per unit mass.

$$SEA = \frac{EA}{m} \quad (2)$$

Energy absorption efficiency (E_f) is defined by Eq. (3), H representing the total height of the specimen. The displacement when the E_f curve obtains the last extreme value within the deformation phase is

defined as the densification displacement (u_d). Due to the different deformation modes of the structure, u_d varies and is not a constant value.

$$E_f = \frac{EA}{H \bullet f(u)} \quad (3)$$

$$\left. \frac{dE_f}{du} \right|_{u=u_d} = 0 \quad (4)$$

The mean crushing force (MCF) is expressed as Eq. (5). This denotes the average compressive force applied to the specimen prior to densification displacement.

$$MCF = \frac{EA}{u_d} \quad (5)$$

Additionally, during the processing of the experimental data, the normalized displacement, u/H , is used for characterization to ensure consistency in comparisons.

4. Results of the experiment

4.1. Results of T-cell

The force-normalized displacement and deformation processes of the T-cell under various conditions are depicted in Figs. 6 and 7. The deformation process delineates into four stages: elastic, reinforcement, yield, and densification stages. For the hollow T-cell, the reinforcement stage can be subdivided into two sub-stages: the first reinforcement segment results from the protruding regions on the left and right sides coming into contact with each other, and the latter reinforcement segment results from the transition regions on the top and bottom sides coming into contact with each other. Specifically, Fig. 7(a) illustrates that at $u/H = 0.78$, the concave region of the hollow T-cell connected to

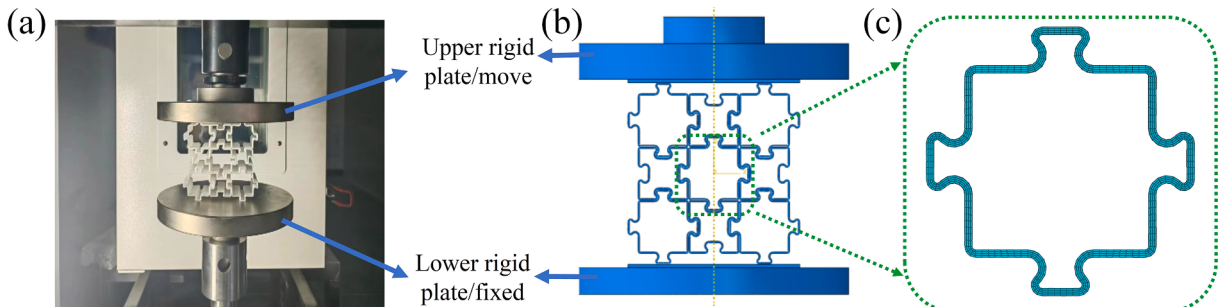


Fig. 5. Quasi-static experimental loading: (a) experimental setup, (b) finite mode, (c) division of the grid.

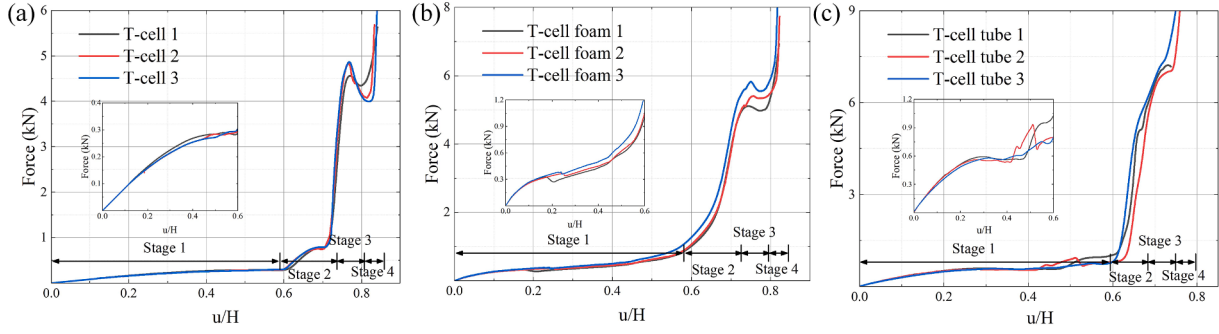


Fig. 6. Quasi-static compression force-normalized displacement curves of T-cell at different conditions: (a) hollow, (b) foam, (c) tube.

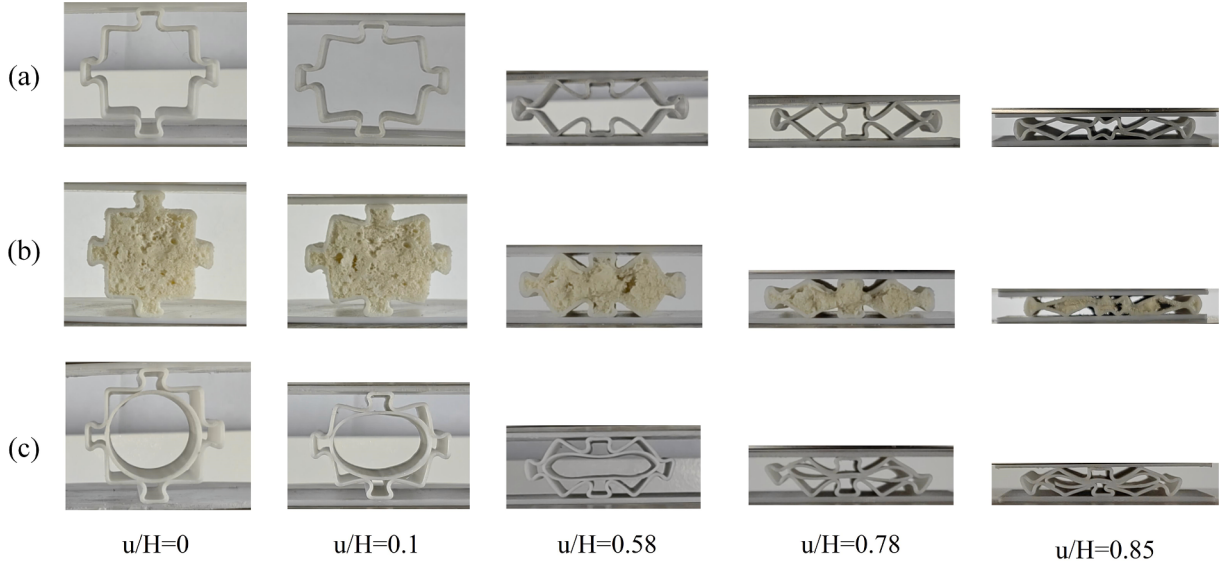


Fig. 7. Quasi-static compressive deformation process of T-cell under different conditions: (a) hollow, (b) foam, (c) tube.

the rigid plates expands laterally, leading to structural yielding in this area, which diminishes the load-bearing capacity. Fig. 6(b) clearly shows that the force-normalized curves of the T-cell foam remain smooth during the reinforcement and yielding stages, without significant stepwise increases in force values. Notably, in Stage 3, the force curve does not exhibit a significant drop but instead maintains a modest plateau. This stability is attributed to the supportive effect of the filled foam on the cell wall, enabling a more gradual yielding process in the concave area connected to the rigid plates, thereby enhancing the energy absorption of the T-cell foam during this stage. This observation is further corroborated by the force values in Stage 1, where the load-bearing capacity of the T-cell foam surpasses that of the hollow T-cell.

The force-normalized displacement of the T-cell tubes are depicted in Fig. 6(c). In contrast to the first two sets of experimental conditions, the strengthening stage of the T-cell tubes demonstrates a rapid increase in force. This phenomenon is attributed to the extrusion and deformation of the tubes towards both sides under increased displacement load. Simultaneously, the tubes are internally tangent to the T-cell, and the deformed tubes are inserted into the concave regions on both sides of the T-cells, as illustrated in Fig. 7(c). This significantly enhances the load-bearing capacity of the cell. Nevertheless, the tube impedes the overall deformation of the T-cell; there is a swift increase in the force value and densification of the overall system. This assertion is validated through the yield stage, as evident from the force-normalized displacement curves, wherein the T-cell tube fails to exhibit a prominent plateau during the buckling stage. Owing to operational errors during testing, T-cell tube 1 experienced an interruption and failed to reach the

densification stage; however, the remaining three stages exhibited consistency with T-cell tube 2, confirming the experimental data as usable.

The SEA and E_f for the T-cell under three conditions are depicted in Fig. 8. Analysis of the SEA shows a gradual increase followed by a rapid ascent, corresponding to Stage 2's sharp force increase in the force-normalized displacement curves. Fig. 8(b) indicates a reduction in the u_d of the T-cell, due to the filling with foam and tubes, with tubes exerting a more significant impact. However, filling tubes substantially enhance the system's load-bearing capacity, and the statistical outcomes are presented in Table 3.

4.2. Results of A-cell

The force-normalized displacement and deformation processes of the A-cell under three conditions are illustrated in Figs. 9 and 10. Upon analyzing the force-normalized displacement of the hollow A-cell and A-cell foam, the deformation process is categorized into five stages: elastic, stable, reinforcement, plastic, and densification. Fig. 10(a) and (b) reveal that during deformation, the concave areas on both sides of the A-cell cave inward, illustrating a negative Poisson's ratio effect in the overall structural deformation, thereby enhancing the load-bearing capacity of the A-cell. The experimental hollow A-cell exhibits a centrosymmetric deformation pattern instead of the ideal axisymmetric deformation pattern, which is due to errors in the preparation of the specimens, resulting in uneven forces during the loading process. Analysis of Fig. 10(b) reveals that after filling the foam in the hollow

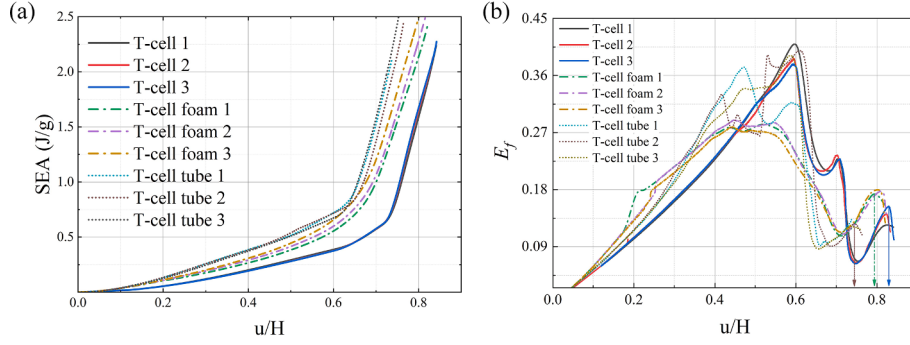


Fig. 8. (a) Specific energy absorption (b) Energy absorption efficiency of T-cells.

Table 3
SEA and MCF under different conditions of T-cells.

Specimen	Mass (g)	u_d (mm)	Average densification u/H	SEA (J/g)	Average SEA (J/g)	MCF (kN)	Average MCF (kN)
T-cell 1	12.76	34.59	0.834	1.94	1.98	0.716	0.729
T-cell 2	12.73	34.61		1.98		0.728	
T-cell 3	12.74	34.85		2.03		0.742	
T-cell foam 1	17.43	33.35	0.800	2.07	2.15	1.082	1.112
T-cell foam 2	18.12	33.60		2.21		1.192	
T-cell foam 3	17.86	33.99		2.16		1.135	
T-cell tube 1	18.85	31.28	0.740	2.23	2.31	1.344	1.395
T-cell tube 2	18.79	30.97		2.31		1.401	
T-cell tube 3	18.74	30.97		2.38		1.440	

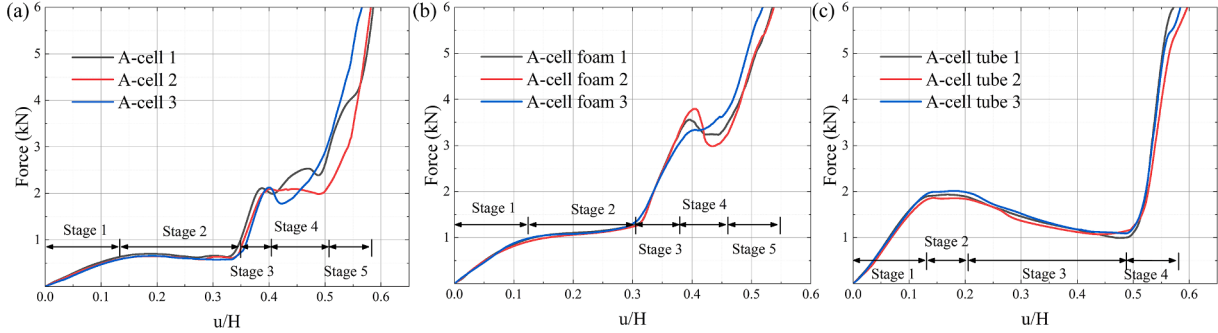


Fig. 9. Quasi-static compression force-normalized displacement curves of A-cell at different conditions:(a) hollow, (b) foam, (c) tube.

region of the A-cell, the foam filling provides substantial support to the cell wall surface, leading to a notable enhancement in the load-bearing capacity during the stable stage compared to that of the hollow A-cell. At the same time, the defects in the A-cell preparation process are cancelled out due to the inward compression of the foam, and the system exhibits an axisymmetric deformation pattern, which greatly improves the energy absorption.

Unlike the deformation process observed in the hollow A-cell and A-cell foam, the A-cell tube exhibits four stages. Stages 1 and 2 agree with the other two sets of experiments, representing the elastic and stable stages. After filling the tube, the reinforcing effect in these two stages proves superior to that observed with foam filling. Significant differences emerge at Stage 3, the deformation process clearly shows that the tube undergoes torsion along the diagonal during compression, extending between the concave areas on both sides of the diagonal. As displacement load increases, the tube causes the concave areas on both sides to deform in a centrally symmetric manner. This leads to the concave areas on the left and right sides not contacting those on the top and bottom sides, greatly reducing the structural load-bearing capacity and ultimately decreasing the force experienced at Stage 3.

The SEA and E_f for the A-cell under different conditions are presented

in Fig. 11, respectively. From Fig. 11(a), it is observed that the SEA of the A-cell tube initially increases more rapidly and then slows down compared to A-cell foam. This trend is attributed to the deformation mode of the A-cell tube in Stage 3, where the tube decreases its load-bearing capacity, resulting in a rapid decline in SEA. Analysis of Fig. 11(b) reveals that the tube induces centrally symmetrical deformation in A-cell, and the compression of foam in the A-cell foam accumulates toward the center, resulting in a densification displacement that is greater than that of A-cell foam. The SEA and MCF values are shown in Table 4.

4.3. Results of JMSS

The force-normalized displacement and deformations of JMSS under three conditions are depicted in Figs. 12 and 13. The force-normalized displacement of hollow JMSS is depicted in Fig. 12(a), delineating its deformation process into four stages: elastic, reinforcement, plateau, and densification. However, the strong support of foam on the central cells of JMSS impedes the complete deformation of the system, at $u/H = 0.54$, the overall system becomes dense, resulting in a loss of its energy absorption capacity. Nevertheless, after foam filling, the curve exhibits

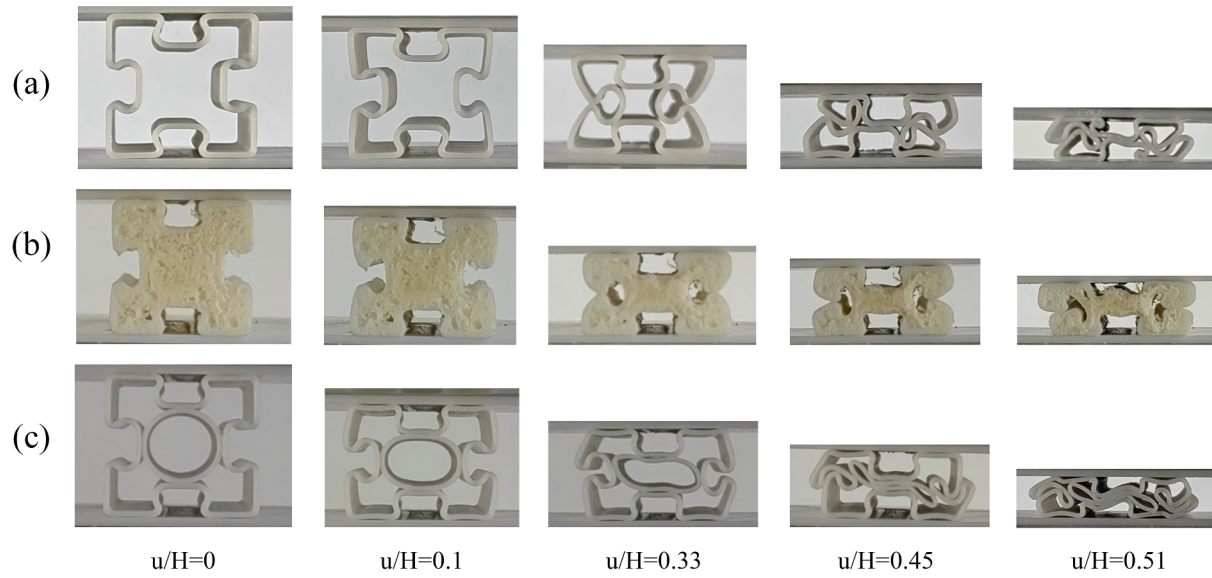


Fig. 10. Quasi-static compressive deformation process of A-cell under different conditions: (a) hollow, (c) foam, (d) tube.

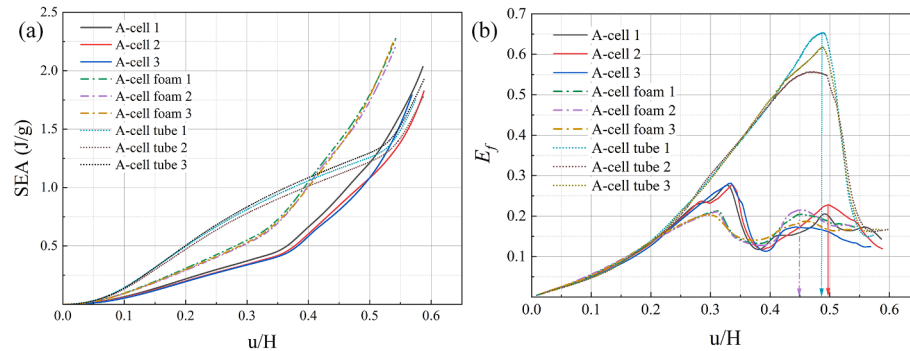


Fig. 11. (a) Specific energy absorption (b) Energy absorption efficiency of A-cells.

Table 4
SEA and MCF under different fillers of A-cells.

Specimen	Mass (g)	u_d (mm)	Average densification u/H	SEA (J/g)	Average SEA (J/g)	MCF (kN)	Average MCF (kN)
A-cell 1	12.75	14.75	0.484	1.17	1.06	1.011	0.923
A-cell 2	12.73	14.71		1.07		0.926	
A-cell 3	12.72	14.12		0.93		0.838	
A-cell foam 1	14.46	13.55	0.455	1.41	1.40	1.505	1.495
A-cell foam 2	14.69	13.53		1.36		1.477	
A-cell foam 3	14.55	13.84		1.43		1.503	
A-cell tube 1	15.89	14.69	0.484	1.24	1.26	1.341	1.388
A-cell tube 2	15.90	14.23		1.17		1.307	
A-cell tube 3	15.88	14.64		1.26		1.367	

smoother characteristics without distinct inflection points, as depicted in Fig. 12(b). The curves and deformation of the JMSS tubes are significantly different from those of the hollow JMSS, and the deformation process is divided into five stages, with Stages 1, 3, and 5 representing the elastic, reinforced, and dense stages, respectively, as in the hollow JMSS. Stages 2 and 4 are two platform segments: the first one is generated because of the deformation of the tube tangent to the T-cell, and the second one is generated because of the deformation of the tube tangent to the A-cell. Since the diameter of the tube tangent to the T-cell is larger than that of the tube tangent to the A-cell, the displacement in Stage 2 is larger than that in Stage 4. The force-normalized displacement curves of the JMSS tube show more drastic fluctuations, due to the local

damage of the PLA during the loading process. From the deformation of JMSS under the three conditions, the T-cell deformation in JMSS exhibits the effect of negative Poisson's ratio, resulting in the overall deformation showing inward concave characteristics, significantly enhancing its load-bearing capacity and energy-absorbing capabilities.

The SEA and E_f of JMSS under various conditions are illustrated in Fig. 14(a) and (b). Fig. 14(a) clearly demonstrates that the growth of SEA in the JMSS tube surpasses that of JMSS foam, underscoring the superior load-bearing capacity and energy absorption of tubes in JMSS systems. The E_f curve depicted in Fig. 14(b) exhibits two distinct peaks subsequent to tube filling, aligning with the two plateau regions in the force-normalized displacement curve. Additionally, from Eq. (4), it is

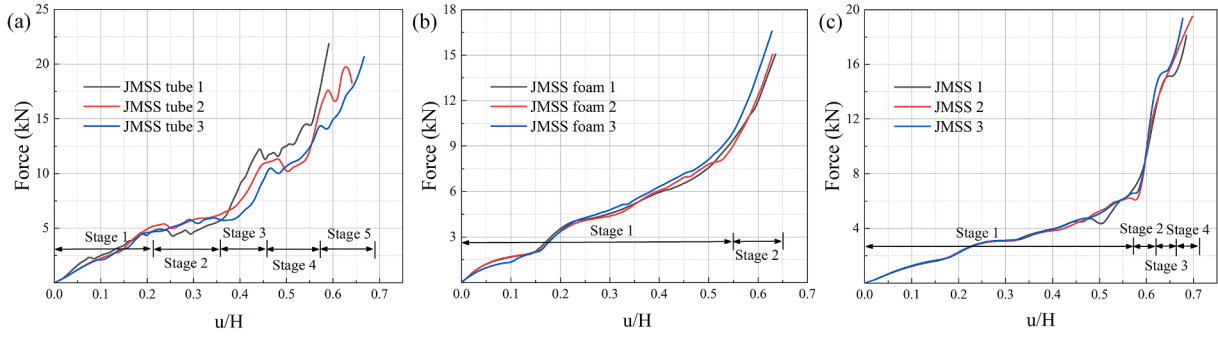


Fig. 12. Quasi-static compression force-normalized displacement curves of JMSS at different conditions:(a) hollow, (b) foam, (c) tube.

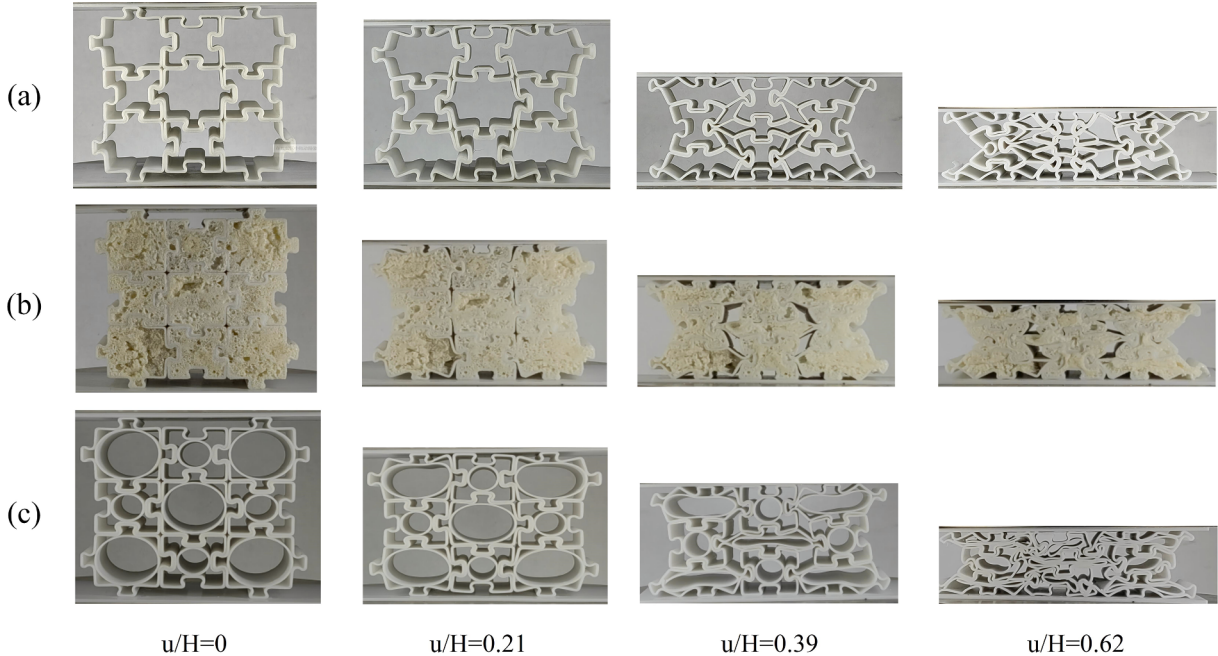


Fig. 13. Quasi-static compressive deformation process of JMSS under different conditions: (a)hollow, (c) foam, (d) tube.

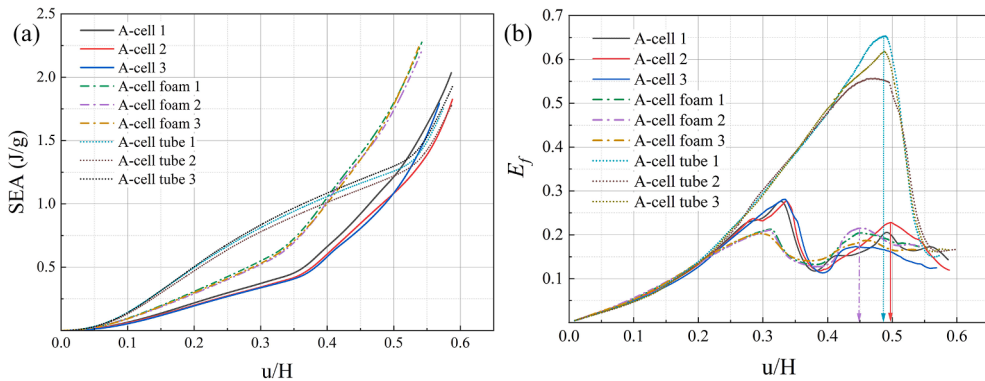


Fig. 14. (a) Specific energy absorption (b) Energy absorption efficiency of JMSS.

inferred that tube filling leads to a reduced densification displacement for JMSS in comparison to foam filling. Both densification displacements are lower than those observed in hollow JMSS. The calculated densification displacements, along with the resultant *SEA* and *MCF* values, are summarized in Table 5.

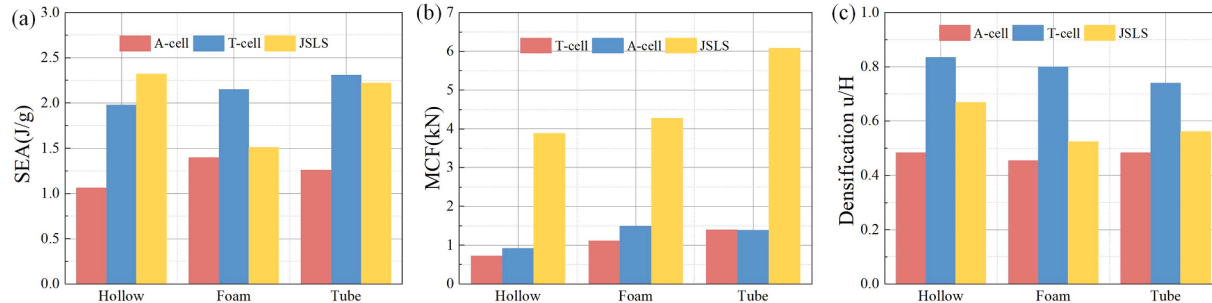
4.4. Comparison of experimental results

The *SEA*, *MCF*, and densification u/H of different specimens under various conditions are analyzed, and the results are shown in Fig. 15. Although the densification u/H of the hollow JMSS is less than that of the T-cell, the *SEA* of the JMSS exceeds that of the T-cell. This suggests that well-assembled interlocking systems enable every cell in JMSS to

Table 5

SEA and MCF under different conditions of JMSS.

Specimen	Mass (g)	u_d (mm)	Average densification u/H	SEA (J/g)	Average SEA (J/g)	MCF (kN)	Average MCF (kN)
JMSS 1	113.36	67.30	0.669	2.24	2.32	3.773	3.888
JMSS 2	114.69	68.21		2.34		3.935	
JMSS 3	114.82	69.21		2.39		3.965	
JMSS foam 1	134.56	52.15	0.525	1.58	1.65	4.077	4.270
JMSS foam 2	138.53	54.33		1.67		4.258	
JMSS foam 3	141.40	54.05		1.71		4.474	
JMSS tube 1	156.79	55.94	0.562	2.21	2.22	6.194	
JMSS tube 2	156.97	53.98		1.99		5.787	6.077
JMSS tube 3	156.95	62.05		2.47		6.248	

**Fig. 15.** Comparison of different specimens with different conditions (a) SEA, (b) MCF, (c) densification u/H.

deform adequately, thereby enhancing the system's energy absorption. However, the SEA of T-cell foam and T-cell tube exceeds that of JMSS, a result primarily due to the addition of filler, which significantly impedes the deformation of JMSS, and the notably lower densification u/H of JMSS compared to that of T-cell foam and T-cell tube. Comparing the key indices of T-cell and A-cell reveals that T-cell's performance under the three working conditions surpasses that of A-cell. This is attributed to T-cell exhibiting a positive Poisson's ratio and higher densification displacement. Although the hollow A-cell and A-cell foam demonstrate a negative Poisson's ratio effect and higher load-carrying capacity in the platform section, their smaller densification displacement weakens their energy absorption. Additionally, the A-cell tube did not fully realize its energy-absorbing potential due to the circular tube-induced torsional deformation of the wall surface. Given that the MCF calculation is based on the energy absorption and displacement during densification, the average MCF of the T-cell is greater than that of the A-cell under various conditions. Moreover, the JMSS outperforms individual cells in all scenarios, highlighting its superior load-bearing capacity.

5. Finite element analysis

5.1. Finite element model

The simulations of JMSS are conducted using ABAQUS/Explicit. The specimen is positioned between two rigid plates, as shown in Fig. 5(b). The lower rigid plate is assumed to be fully constrained in all directions, while the upper rigid plate moves solely downwards and is restrained in other directions. Notably, to reduce the dynamic response of the system, displacement loading is applied to the upper rigid plate using a smooth step in the finite element simulation calculations that employ explicit dynamics [54]. Generic contact is adopted to describe complex contact behavior during loading processes. The tangential behavior defines the friction coefficient as 0.3, and the normal behavior defines the hard contact [30]. An elastic-plastic model is used to describe the mechanical behavior of PLA, and the stress-strain curves from the material tests are imported into ABAQUS. Both the specimen and the rigid plate are meshed with hexahedral elements (C3D8R). The specimen is discretized with a minimum of 4 elements in the thickness direction to ensure the

reliability of the computational calculations, as depicted in Fig. 5(c). Mesh convergence analysis of the T-cell was conducted prior to simulation initiation, with results depicted in Fig. 16 (a). Based on the results, the final mesh size is determined to be 1 mm.

The comparison between the experimental and simulation results of JMSS is illustrated in Fig. 16(b) and (c). The force-normalized displacement curves and the deformation process show the same trend, but the experimental results fluctuate more, and the simulation result is lower, possibly due to the material damage not being considered in the simulation. Moreover, the perfect initial geometries are considered in the simulation, though experiment errors are inevitable. In addition, the setting of the friction coefficient also has some influence on the simulation results.

5.2. Effect of geometric parameters

This section analyzes the impact of geometric parameters JMSS performance using finite element methods. Specifically, the study investigates the effects of cell wall thickness (t), the inclination angle (α) of the abdomen plate, and the depth of concavity/protrusion (h) on various aspects of JMSS, as illustrated in Fig. 2(b) and (c), including its SEA and MCF. Fig. 17 illustrates the force-normalized displacement, SEA and E_f curves of JMSS under varying geometric parameters and Fig. 18 shows the statistical results.

The inclination α of the cell significantly influences on the mechanical behavior of the JMSS. Fig. 17(a)-(c) show that the plateau region in the curves widens with increasing α , leading to higher u_d and improved energy absorption. This effect can be attributed to the fact that a larger α results in a more stable deformation pattern and a more homogeneous stress distribution throughout the system. As the inclination α increases, the load paths in the JMSS are optimized, delaying the onset of densification and leading to more uniform energy absorption throughout the deformation process. As a result, a higher value of α yields a more consistent load response over an extended deformation range.

Fig. 17(d)-(f) demonstrate that an increase h also increases in the u_d , SEA and MCF of the JMSS. Increasing h improves the system interlocking mechanism, increases the area of mutual contact and plastic

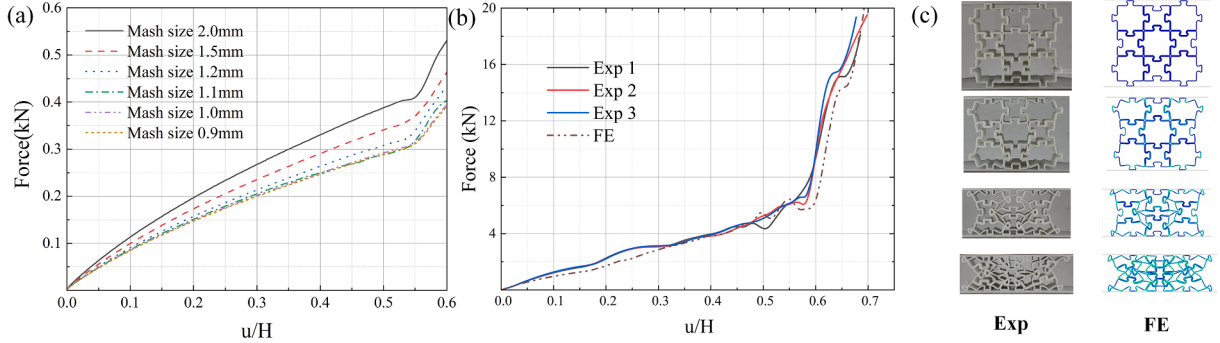


Fig. 16. Finite element simulation verification: (a) convergence analysis of the mesh, (b) comparison of experimental and simulated force-normalized displacement curves for quasi-static compression, (c) deformation process.

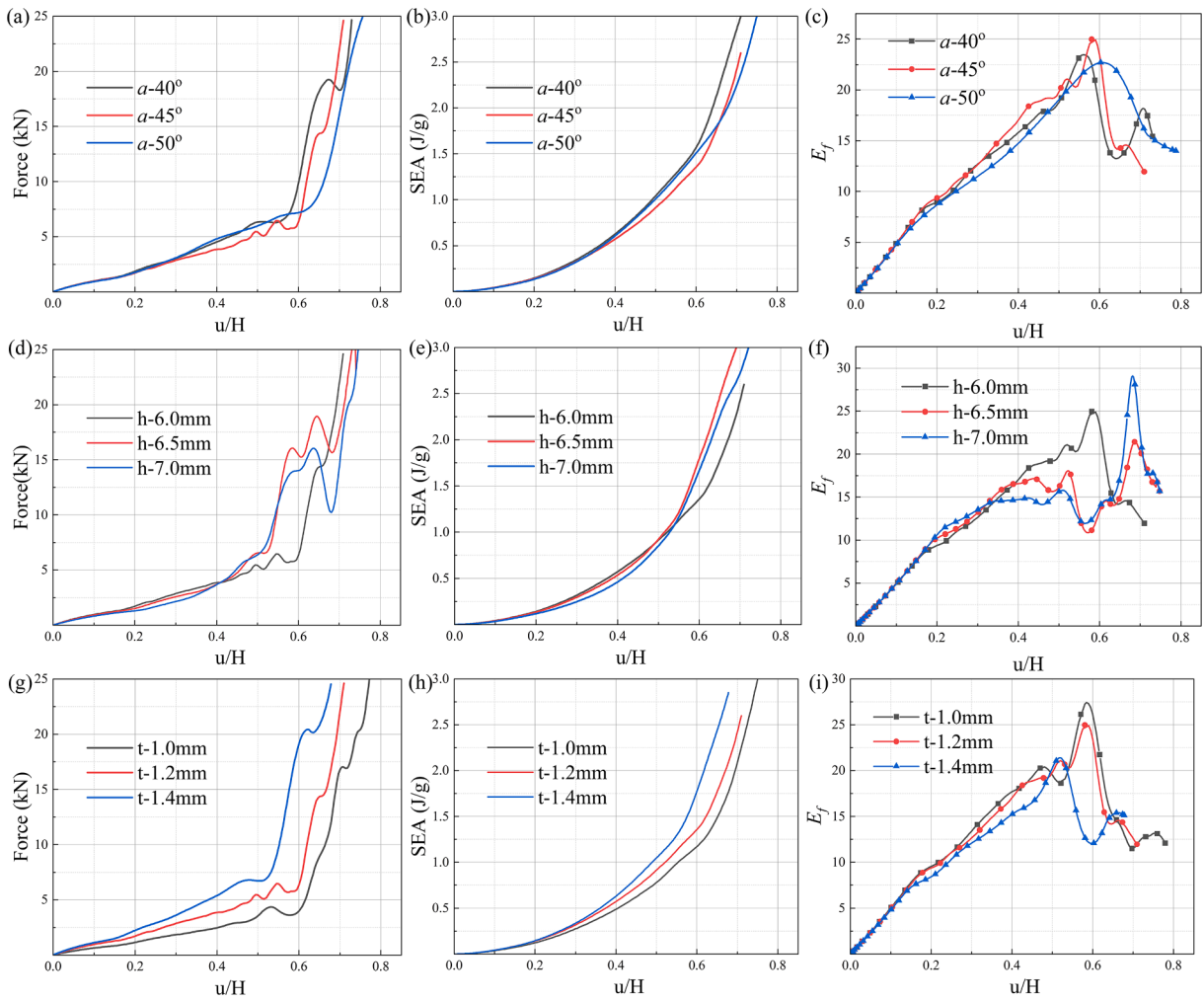


Fig. 17. Force-normalized displacement, SEA and E_f curves of JMSS with different geometrical parameters.

deformation region of T-cells and A-cells, and increases energy dissipation and SEA. However, it also means that larger h values could make the structure prone to premature failure due to increased stress concentrations and flexural deformations.

Regarding the t of cell walls, as illustrated in Fig. 17(g)-(i), it seems that the increase of the t can significantly increase the load carrying capacity of the JMSS throughout the deformation phase. However, the increase in t prevents some regions of the A-cell and T-cell from deforming efficiently, and the energy absorption is generated by the plastic deformation of the system, which leads to a lower SEA of the

JMSS with a larger t . In addition, the increased t also leads to smaller densification displacement, which further reduces its SEA. Because the MCF is calculated using the energy absorption method, although greater t improves load carrying capacity, thicker t reduces the MCF in the effective deformation range.

5.3. Comparison with conventional self-locking system

In this section, comparative simulations are conducted between the JMSS and traditional self-locking systems, as depicted in Fig. 1. These

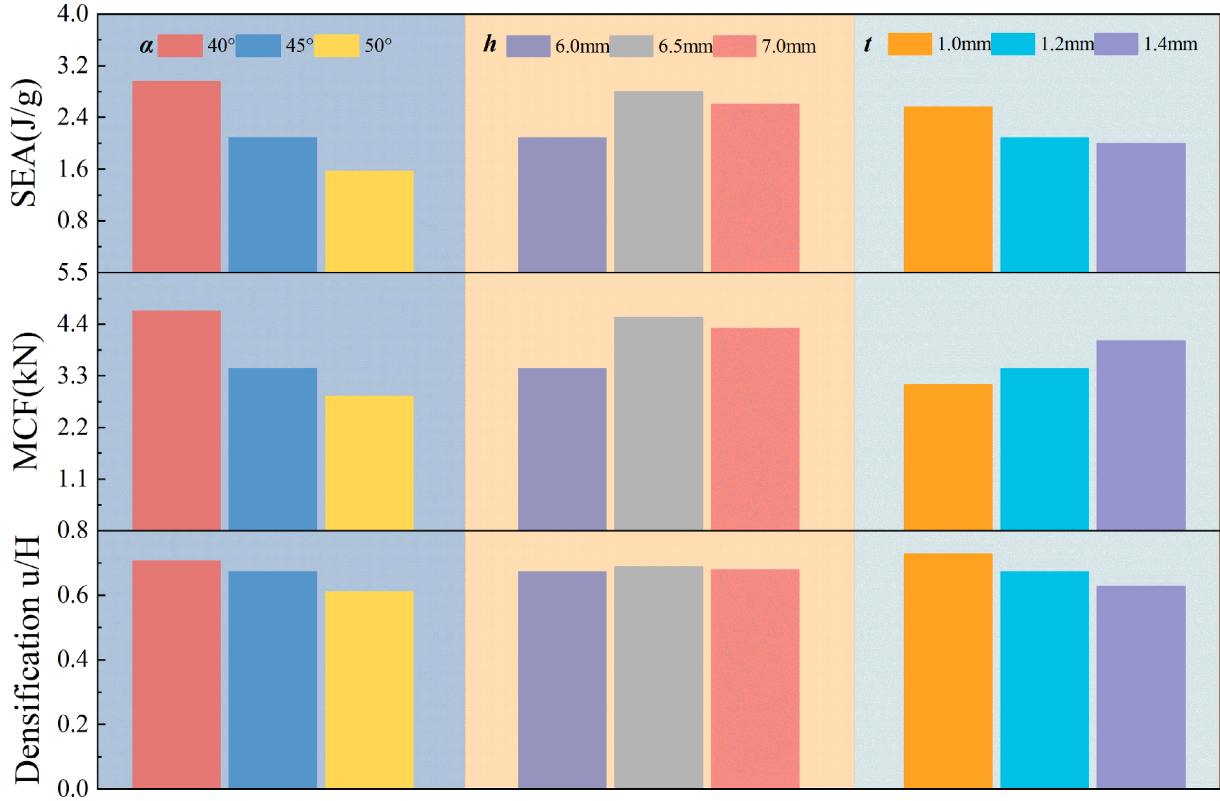


Fig. 18. Key metrics statistics of JMSS with different geometrical parameters.

systems undergo quasi-static flat plate compression simulations in three directions, following the settings outlined in [Section 5.1](#). To ensure better comparability of results, the relative density of each system is kept consistent by adjusting the wall thickness. Here, the relative density ($\bar{\rho}$) is defined as $\bar{\rho} = m/V$ with m representing the actual mass of the system and V representing the geometric volume, and the $\bar{\rho}$ of each system is 0.152 g/cm^3 . The force-normalized displacement curves from the simulation under each direction are shown in [Fig. 19](#). Comparison of the data obtained from loading in the Y direction with those reported in the original literature indicates good consistency, demonstrating the

reliability of the simulations.

It is observed that JMSS exhibits weaker mechanical performance than traditional self-locking systems when loaded in the Y direction, primarily due to the presence of A-cells, which introduce an inward caving effect. This significantly reduces the effective deformation space and lowers the material utilization rate. Consequently, the SEA and densification u/H of JMSS are substantially lower than those of CGTS and DSTS, as shown in [Fig. 19\(d\) and \(f\)](#). However, when loaded in the X direction, traditional self-locking systems such as CGTS and DSTS experience partial cell detachment, resulting in a decrease in load-

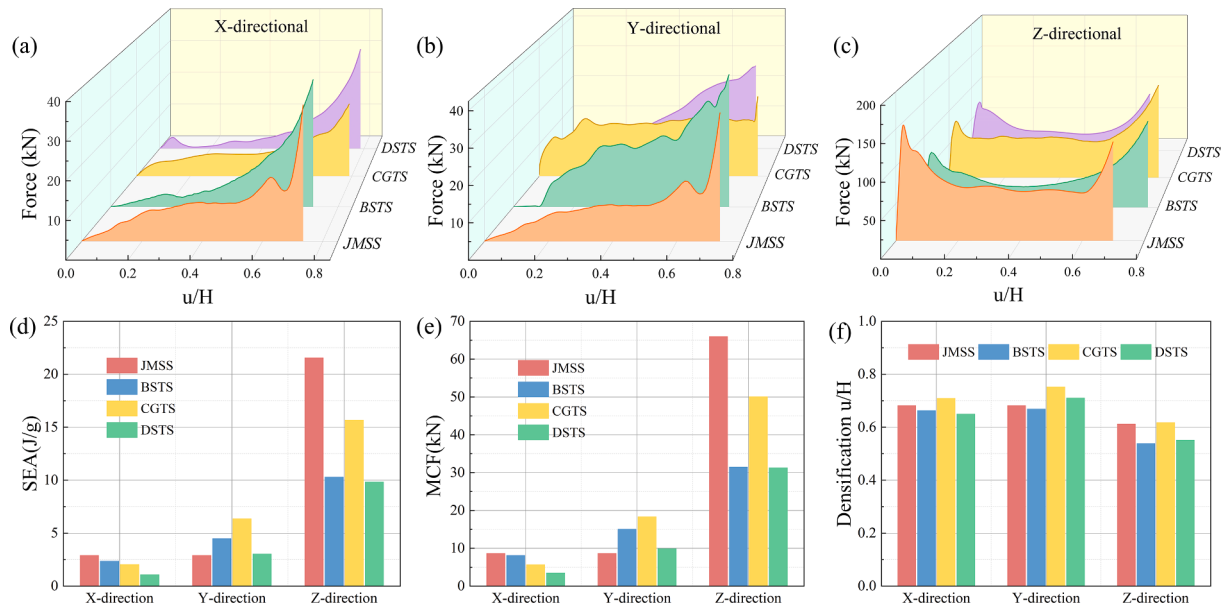


Fig. 19. Performance comparison of several self-locking systems: (a) Y-direction, (b) X-direction, (c) Z-direction, (d) SEA, (e) MCF, (f) densification u/H .

bearing performance. In contrast, the interlocking design of JMSS prevents such detachment, enhancing both its load-bearing and energy absorption capabilities. In the Z direction, all self-locking systems exhibit buckling failure; however, JMSS shows a higher buckling load due to its interlocking cells, as reflected in the peak load seen in Fig. 19 (c). This higher peak load, combined with improved loads in the plateau stage, results in better energy absorption for JMSS compared to the other structures. Additionally, the multidirectional capability of JMSS is further evidenced by its significantly enhanced SEA and MCF in the Z direction.

While traditional self-locking systems may offer better performance under specific conditions, the JMSS demonstrates superior overall energy absorption and load-bearing performance, particularly in the X and Z directions. This comparison underscores the multidirectional robustness of the JMSS, making it a potentially more versatile option than conventional designs in applications where multidirectional load-bearing and energy absorption are critical. Nonetheless, further optimization of the A-cell structure could help mitigate the material inefficiencies observed in the Y direction, enhancing the JMSS's applicability across all loading conditions.

6. Conclusions

This study presents the design a novel Jigsaw-Inspired Multi-Directional Self-Locking System (JMSS), which addresses the limitations of traditional self-locking systems by offering improved energy absorption and multidirectional load-bearing capacity. Additionally, the load-bearing performance of JMSS can be further optimized through the incorporation of foam and tube fillers, enhancing its structural efficiency in various applications. The conclusions drawn from the study are as follows:

- (1) Experiments reveal that the JMSS exhibits higher *SEA* and *MCF* compared to two types of single cells. This indicates that the self-locking mechanism allows each JMSS cell to deform sufficiently, enhancing its energy absorption effect. The A-cell's performance, in terms of *SEA*, *MCF*, and densification u/H , is weaker than the T-cell's due to its negative Poisson's ratio effect during deformation, compared with the positive Poisson's ratio effect exhibited by the T-cell.
- (2) Filling cell cavities with foam and tubes enhances the *SEA* and *MCF* of single cells; however, it severely impacts the structural densification displacement, resulting in a negative energy absorption gain for JMSS. Overall, tubes offer superior enhancement in load-bearing capacity and energy absorption for the T-cell and JMSS compared to foam.
- (3) Simulations investigating geometric parameters show that increasing the α and the h improves the *SEA* and *MCF* of the

Appendix A. Modeling details

JMSS consists of two types of cells (A-cell and T-cell), and the modeling of these elements can be divided into six steps, as illustrated in Figs. A1 and A2. The A-cell and T-cell must be used in conjunction with each other. During the modeling process, the A-cell is modeled inward, while the T-cell faces outward, ensuring that both the modeling process and the dimensions of these cytosolic elements remain consistent. Using the A-cell modeling process as an example, this section describes the modeling process of JMSS cytosolic elements in detail. This section introduces the modeling process of the JMSS cell in detail.

The modeling process for the A-cell is as follows: **Step 1:** Draw a square with a side length of 30 mm, and draw a straight line 6 mm inward along the axis of symmetry, as well as a horizontal line at one end. Create a notch on the side of the square, located 1 mm from the symmetry axis, such that the position of the notch aligns with the direction of the horizontal line. A straight line at a 45° angle from the side length is then drawn at the notch, intersecting with the horizontal line. **Step 2:** Chamfer the corners of the square and the two angles formed by the horizontal line and the edge length, using a chamfer radius of 1.7 mm. **Step 3:** Symmetrize the fillet curve along the axis of symmetry, delete the drawn 6 mm auxiliary line, and trim the excess right-angled edges. **Step 4:** Rotate and copy the arc curve formed on one side length by 90°, using the geometric center of the square. **Step 5:** Rotate and duplicate the arcs formed on both side lengths by 180°, with the geometric center of the square, to obtain the geometric outline of the A-cell. **Step 6:** Utilize the Offset tool to shift the A-cell geometry curve inward by 1.2 mm to complete the planar modeling of the A-cell. To obtain a 3D

system. Increasing the t enhances the *MCF* of JMSS, albeit at the expense of its *SEA*.

- (4) Comparative analysis with traditional self-locking systems under varying load directions indicates that JMSS energy absorption in the Y direction is inferior to that of traditional systems. This is due to the JMSS inward deformation, which significantly impacts its densification displacement. However, in the X and Z directions, the interlocking capability of the cells allows JMSS to exhibit a higher load-bearing capacity and energy absorption compared to traditional systems.

The JMSS offers significant advantages for industries such as aerospace and automotive, where lightweight and high energy-absorbing structures are crucial. Its ability to withstand complex multidirectional loads, while reducing the reliance on additional fasteners, improves both assembly efficiency and structural integrity. The customizable geometry and fillable cavities allow for performance optimization tailored to specific design requirements. Additionally, the modular and replaceable cell design minimizes repair costs following damage, making JMSS a cost-effective and adaptable solution for advanced structural designs in high-demand environments, such as aircraft fuselage reinforcements or automotive crash energy absorbers.

CRediT authorship contribution statement

Yao-Yao Xu: Writing – original draft, Visualization, Validation, Software, Methodology, Investigation, Formal analysis, Data curation. **Jin-Shui Yang:** Writing – review & editing, Supervision, Project administration, Methodology, Investigation, Funding acquisition, Conceptualization. **Hao Han:** Visualization, Validation, Methodology, Investigation, Conceptualization. **Peng Yin:** Methodology, Investigation. **Shuang Li:** Validation, Methodology, Investigation, Conceptualization. **Xu-Chang Liu:** Visualization, Investigation, Conceptualization. **Hong-Ze Li:** Methodology, Investigation. **Jing Gao:** Software, Methodology, Investigation.

Declaration of competing interest

The authors declare that they have no known competing financial interests or personal relationships that could have appeared to influence the work reported in this paper.

Acknowledgments

The present work was supported by the National Natural Science Foundation of China under Grant No. 12172098.

structure, after completing the planar work, stretch it perpendicular to the plane's direction according to the required length.

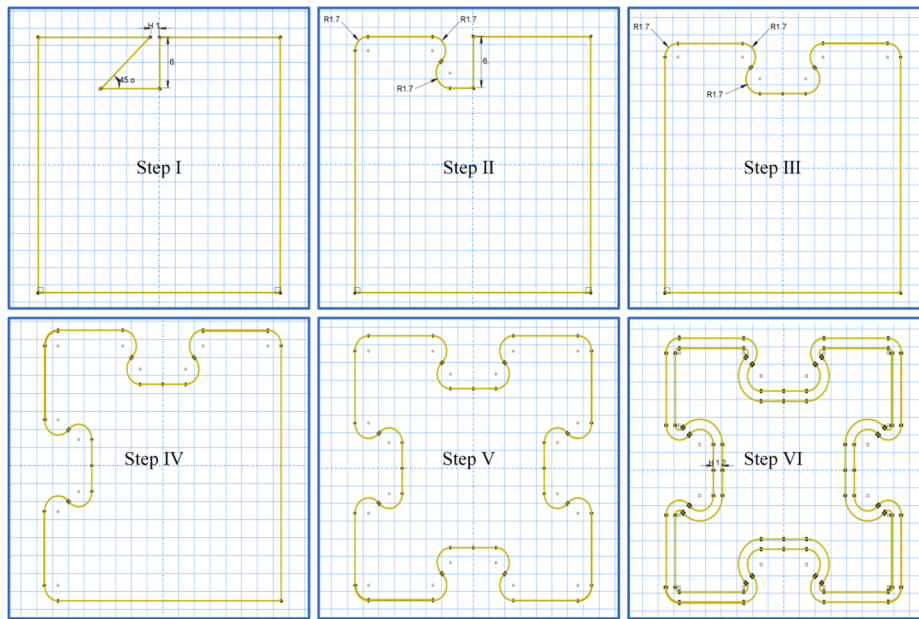


Fig. A1. Modeling process of the A-cell.

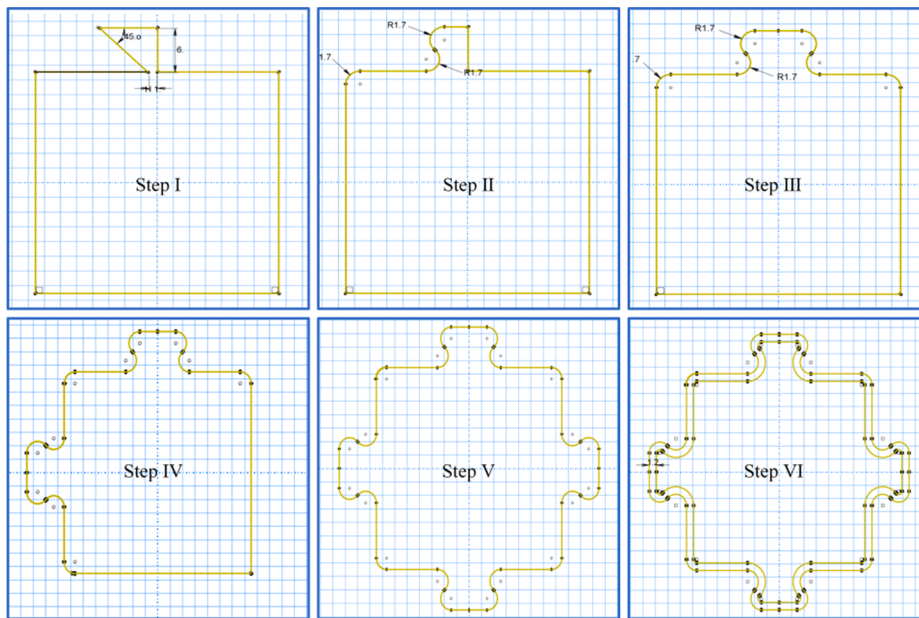


Fig. A2. Modeling process of the T-cell.

Data availability

Data will be made available on request.

References

- [1] Xiao Z, Gao P, He X, Qu Y, Wu L. Lightweight cellular multifunctional metamaterials with superior low-frequency sound absorption, broadband energy harvesting and high load-bearing capacity. Mater Des 2024;241:112912.
- [2] Zhu L, Li N, Childs PRN. Light-weighting in aerospace component and system design. Propul Power Res 2018;7:103–19.
- [3] Chen D, Yan R, Lu X. Mechanical properties analysis of the naval ship similar model with an integrated sandwich composite superstructure. Ocean Eng 2021;232:109101.
- [4] Zhang W-M, Li Z-Y, Yang J-S, Ma L, Lin Z, Schmidt R, et al. A lightweight rotationally arranged auxetic structure with excellent energy absorption performance. Mech Mater 2022;166:104244.
- [5] Gärtner T, Van Den Boom SJ, Weerheijm J, Sluys LJ. Geometric effects on impact mitigation in architected auxetic metamaterials. Mech Mater 2024;191:104952.
- [6] Lin H-B, Liu H-T, An M-R. In-plane dynamic impact behaviors of a self-similar concentric star honeycomb with negative Poisson's ratio. Mater Today Commun 2022;33:104474.
- [7] Ye M, Gao L, Li H. A design framework for gradually stiffer mechanical metamaterial induced by negative Poisson's ratio property. Mater Des 2020;192:108751.

- [8] Darwish Y, ElGawady MA. Numerical and experimental investigation of negative stiffness beams and honeycomb structures. *Eng Struct* 2024;301:117163.
- [9] Gan J, Li F, Li K, Li E, Li B. Dynamic failure of 3D printed negative-stiffness meta-sandwich structures under repeated impact loadings. *Compos Sci Technol* 2023;234:109928.
- [10] Tan X, Wang B, Wang L, Zhu S, Chen S, Yao K, et al. Effect of beam configuration on its multi-stable and negative stiffness properties. *Compos Struct* 2022;286:115308.
- [11] Liu Y, Wang Y, Ren H, Meng Z, Chen X, Li Z, et al. Ultrastiff metamaterials generated through a multilayer strategy and topology optimization. *Nat Commun* 2024;15:2984.
- [12] Zhang J, Sato Y, Yanagimoto J. Homogenization-based topology optimization integrated with elastically isotropic lattices for additive manufacturing of ultralight and ultrastiff structures. *CIRP Ann* 2021;70:111–4.
- [13] Chen X, Ji Q, Wei J, Tan H, Yu J, Zhang P, et al. Light-weight shell-lattice metamaterials for mechanical shock absorption. *Int J Mech Sci* 2020;169:105288.
- [14] Liu H, Chen L, Cao J, Chen L, Du B, Guo Y, et al. Axial compression deformability and energy absorption of hierarchical thermoplastic composite honeycomb graded structures. *Compos Struct* 2020;254:112851.
- [15] Mancini E, Utzeri M, Farotti E, Lattanzi A, Sasso M. DLP printed 3D gyroid structure: Mechanical response at meso and macro scale. *Mech Mater* 2024;192:104970.
- [16] Wu W, Liu P, Wang Y, Kang Z. Design of dual-material lattice structures with compression-torsion bi-stability. *Mater Des* 2023;230:111996.
- [17] Kwon Y, Seo SE, Lee J, Berezvai S, Read De Alaniz J, Eisenbach CD, et al. 3D-printed polymer foams maintain stiffness and energy dissipation under repeated loading. *Compos Commun* 2023;37:101453.
- [18] Zhang J, Lu G, You Z. Large deformation and energy absorption of additively manufactured auxetic materials and structures: A review. *Compos B Eng* 2020;201:108340.
- [19] Acanfora V, Sellitto A, Russo A, Zarrelli M, Riccio A. Experimental investigation on 3D printed lightweight sandwich structures for energy absorption aerospace applications. *Aerospace Sci Technol* 2023;137:108276.
- [20] Wang W-J, Zhang W-M, Guo M-F, Yang J-S, Ma L. Energy absorption characteristics of a lightweight auxetic honeycomb under low-velocity impact loading. *Thin-Walled Struct* 2023;185:10577.
- [21] Li T, Li Y. Mechanical behaviors of three-dimensional chiral mechanical metamaterials. *Compos B Eng* 2024;270:111141.
- [22] Ding L, Zhang D, Yang H, Dong J, Liao B. Curve beam for strengthening the negative Poisson's ratio effect of rotating auxetic metamaterial: Experiments and simulations. *Mater Today Commun* 2024;38:107810.
- [23] Liang L, Yan L, Cao M, Ji Z, Cheng L, Huang R, et al. Microwave absorption and compression performance design of continuous carbon fiber reinforced 3D printing pyramidal array sandwich structure. *Compos Commun* 2023;44:101773.
- [24] Shirzad M, Bodaghi M, Oh D, Yi M, Nam SY. Design and optimization of bioinspired auxetic structure for biomedical applications. *Eur J Mech A Solids* 2024;103:105139.
- [25] Deng Y, Wang Y, Niu Y, Feng Z, Wei G. Research on the influence of foaming silica gel on low-velocity impact performance of M-type GFRP foldcore sandwich structure. *Mech Adv Mater Struct* 2024;1–16.
- [26] Carlson J, Deshpande VS, Fleck NA. The compressive response of the filled Kelvin foam. *Eur J Mech A Solids* 2024;104:105018.
- [27] Wattad O, Grisaro HY. On the efficiency of uniform aluminum foam as energy-absorbing sacrificial cladding for structural blast mitigation. *Eng Struct* 2024;308:118047.
- [28] Azimi MB, Asgari M. A new bi-tubular conical-circular structure for improving crushing behavior under axial and oblique impacts. *Int J Mech Sci* 2016;105:253–65.
- [29] Liu Y-Z, Li S, Lin X, Yang J-S, Li Y, Jiang X-W, et al. Dynamic response of composite tube reinforced porous polyurethane structures under underwater blast loading. *Int J Impact Eng* 2023;173:104483.
- [30] Xie S, Zheng S, Zhang J, Liu Z, Wang H, Zhou H. Study on the crashworthiness of multi-cell thin-walled tubes filled with triply periodic minimal surface lattices. *Mech Adv Mater Struct* 2024;1–17.
- [31] Xiang Y, Yu T, Yang L. Comparative analysis of energy absorption capacity of polygonal tubes, multi-cell tubes and honeycombs by utilizing key performance indicators. *Mater Des* 2016;89:689–96.
- [32] Yao X, Liu K, Dong Q, Li X, Ma C, Hu N. Tunable and recoverable energy absorption of foam-embedded architected cellular composite material at multiple strain rates. *Compos Struct* 2024;329:117745.
- [33] Chen BC, Zou M, Liu GM, Song JF, Wang HX. Experimental study on energy absorption of bionic tubes inspired by bamboo structures under axial crushing. *Int J Impact Eng* 2018;115:48–57.
- [34] Zhang Q, Li B, Zhou S, Luo M, Han F, Chai C, et al. Superior energy absorption characteristics of additively-manufactured hollow-walled lattices. *Int J Mech Sci* 2024;264:108834.
- [35] Wu W, Liu P, Wang Y, Kang Z. Design of dual-material lattice structures with compression-torsion bistability. *Mater Des* 2023;230:111996.
- [36] He X, Huang Z, Chen Z, Li Y. Dynamic response of CFRP-lattice sandwich structures subjected to underwater shock wave loading. *Thin-Walled Struct* 2022;181:109537.
- [37] Deng J, Zhao W, Wang J, Li J, Wu B, Li X, et al. A novel design of an I-shape self-locked thin-walled system with mortise and tenon joints. *Thin-Walled Struct* 2024;201:111966.
- [38] Chen Z, Wei X, Yang L, Xiong J. Origami-based bidirectional self-locking system for energy absorption. *J Mech Phys Solids* 2024;188:105672.
- [39] Li J, Sui C, Sang Y, Zhou Y, Zang Z, Zhao Y, et al. A flexible, reusable and adjustable high-performance energy absorption system inspired by interlocking suture structures. *Int J Solids Struct* 2024;296:112839.
- [40] Chen Y. A novel self-locked energy absorbing system. *Solids: J. Mech. Phys.* 2016.
- [41] Qiao C. Theoretical analysis on the collapse of dumbbell-shaped tubes. *Int J Mech Sci* 2017.
- [42] K. Yang, Internally nested self-locked tube system for energy absorption, (2017).
- [43] Yang K. Shape and geometry design for self-locked energy absorption systems. *Int J Mech Sci* 2019.
- [44] Pan J, Zhu W, Yang K, Hu L, Chen Y. Energy absorption of discretely assembled composite self-locked systems. *Compos Struct* 2022;292:115686.
- [45] Zhang H, Zhang X. Axial crushing of self-lock multi-cell tubes with foam filler and tube envelope. *Thin-Walled Struct* 2020;155:106847.
- [46] Chen Z, Wu Q, Yang H, Yang L, Xiong J. A periodic dissipative system with self-locking capacity. *Int J Impact Eng* 2022;166:104233.
- [47] Zhu Y, Gao D, Shao Y, Chen H, Yu C, Wang Q. A novel prefabricated auxetic honeycomb meta-structure based on mortise and tenon principle. *Compos Struct* 2024;329:117782.
- [48] Liu H, Qiao C, Ma Y, Pan F, Chen Y. A concave-convex design strategy for periodic self-locked energy-absorbing systems. *Int J Impact Eng* 2023;175.
- [49] Yang K, Rao L, Hu L, Pan F, Yin Q, Chen Y. Flexible, efficient and adaptive modular impact-resistant metamaterials. *Int J Mech Sci* 2023;239:107893.
- [50] Yang K, Hu X, Pan F, Qiao C, Ding B, Hu L, et al. An on-demand tunable energy absorption system to resolve multi-directional impacts. *Int J Solids Struct* 2023;271–272:112257.
- [51] Zhao Y. Improving energy absorption of bidirectional self-locked structures and systems inspired by origami crease, European. *J Mech* 2023.
- [52] Zhao Y, Chen L, Wu Z, Du B, Chen L, Li W, et al. Lateral crushing behavior of novel carbon fiber/epoxy composite bidirectional self-locked thin-walled tubular structure and system. *Thin-Walled Struct* 2020;157:107063.
- [53] Zhao Y, Chen L, Du B, Liu H, Chen B, Peng S, et al. Bidirectional self-locked energy absorbing system: Design and quasi-static compression properties. *Thin-Walled Struct* 2019;144:106366.
- [54] Li S, Yang J-S, Schmidt R, Wu L-Z, Schröder K-U. Compression and hysteresis responses of multilayer gradient composite lattice sandwich panels. *Marine Struct* 2021;75:102845.